

# **Green Exfoliation of Van der Waals–Based Magnetic Nanocomposites for Hyperthermia Applications.**

**J. Caland<sup>1</sup>, A. Silva<sup>2</sup>, J. Marroquin<sup>1</sup>, M. H. Sousa<sup>2</sup>, B. S. Archanjo<sup>3</sup>, P. Karagiannidis<sup>4</sup>, and J. F. Felix<sup>1\*</sup>**

<sup>1</sup>Institute of Physics, LabINS, University of Brasília, Brasília-DF, 70910-900, Brazil

<sup>2</sup>Green Nanotechnology Group, University of Brasília, Ceilândia- DF, 72220-275, Brazil.

<sup>3</sup>Materials Metrology Division, National Institute of Metrology, Quality and Technology, Duque de Caxias, Rio de Janeiro, 25250-020, Brazil.

<sup>4</sup>School of Computer Science and Engineering, Faculty of Business and Technology, University of Sunderland, Sunderland, SR6 0DD, United Kingdom.

\*Corresponding author: Tel+55 61931077700 Email address:jorlandio@unb.br (J.F.Felix)

## **Abstract**

We present the development of novel nanocomposites consisting of van der Waals (vdW) materials (WS<sub>2</sub>, MoS<sub>2</sub>, MoSe<sub>2</sub>, TiS<sub>2</sub>, and graphene), maghemite nanoparticles (MNPs), and a gum arabic (GA) matrix, optimized for magnetic hyperthermia applications. These superparamagnetic nanocomposites were comprehensively investigated using a range of advanced characterization techniques. It was found that the incorporation of MNPs enhances the exfoliation efficiency of vdW materials. Transmission electron microscopy revealed that the MNPs, with an average diameter of  $\langle D_{\text{TEM}} \rangle = 8.3 \pm 0.1$  nm, are nearly spherical and uniformly anchored on the surfaces of the vdW material flakes. Raman spectroscopy confirmed the presence of characteristic 2D material signatures and verified the formation of magnetic nanocomposites with varying layer numbers. Zeta potential measurements indicated high colloidal stability, which is essential for biomedical applications.

Magnetic measurements confirmed the superparamagnetic nature of the vdW-integrated nanocomposites, showing reduced saturation magnetization, increased coercivity, and a shifted blocking temperature due to dipole–dipole interactions influenced by the presence of vdW materials. The highest specific absorption rate (SAR) values recorded were 21.4 W/g for Graphene@GA@MNPs, 20.6 W/g for WS<sub>2</sub>@GA@MNPs, and 23.3 W/g for TiS<sub>2</sub>@GA@MNPs. Magnetic hyperthermia tests demonstrated efficient heat generation under alternating magnetic fields, reinforcing their potential for biomedical applications.

**Keywords:** Nanocomposite, Transition Metal Dichalcogenides (TMDs), graphene, superparamagnetic, magnetic hyperthermia

## 1.Introduction

Van der Waals (vdW) materials have emerged as one of the most transformative and rapidly evolving frontiers in nanotechnology [1]. Characterized by their atomic-scale thickness and weak interlayer interactions, these materials exhibit extraordinary properties that distinguish them from conventional three-dimensional systems. Their inherently low-dimensional nature enables the exploration of unique physical and chemical phenomena, driving advancements in electronics, energy storage, and sensing technologies [1–6]. Notably, they are also promising candidates for nanomedical and theranostic applications due to their distinctive optical, electronic, and magnetic properties. Transition Metal Dichalcogenides (TMDs) such as MoS<sub>2</sub>, WS<sub>2</sub>, MoSe<sub>2</sub>, and TiS<sub>2</sub> exhibit tunable thermal conductivity, spin-orbit coupling, and phonon interactions, making them highly suitable for magnetic hyperthermia (MHT) [3,7].

MoS<sub>2</sub> exhibits intrinsic bactericidal activity [8]. Additionally, it provides strong near-infrared (NIR) absorption and tunable thermal anisotropy, enhancing localized heat generation in magneto-photothermal therapies, which supports bacterial inactivation

through thermal stress. Furthermore, MoS<sub>2</sub> reinforces its role in combined magneto-photothermal therapies through its strong NIR absorption and tunable thermal anisotropy [7]. MoSe<sub>2</sub>, with its enhanced spin-orbit coupling and lower bandgap (~1.55 eV) compared to MoS<sub>2</sub> (~1.9eV) for monolayers, facilitates improved phonon-assisted heating under an alternating magnetic field (AMF) [9]. TiS<sub>2</sub>, a novel candidate for MHT, exhibits metallic conductivity and high thermal transport, ensuring efficient heat dissipation and magnetic response [10]—a feature not previously explored in this context. Besides this, studies in the literature have shown that TMDs studied in this work exhibit low toxicity towards human immune cells, such as macrophages, neutrophils, and dendritic cells in the biomedical area. For MoSe<sub>2</sub>, in vitro experiments indicate negligible cytotoxicity, while TiS<sub>2</sub>, particular in PEGylated TiS<sub>2</sub> nanoplates, exhibited low cytotoxicity, maintaining high cell viability even at concentrations up to 80 µg/mL in 4T1 murine breast cancer cells [11,12]. Likewise, graphene and its derivatives, such as magnetic nanoparticle (MNP)-functionalized graphene, exhibit enhanced heat generation under NIR laser irradiation and enable controlled drug release systems [13–14].

MNPs, particularly Fe<sub>3</sub>O<sub>4</sub> and  $\gamma$ -Fe<sub>2</sub>O<sub>3</sub>, are widely used in MHT due to their superparamagnetic behavior, high SAR, and biocompatibility [15]. In addition, they enable precise control via magnetic fields without residual magnetization after field removal [15,16]. Integrating MNPs with TMDs provides synergistic benefits, including improved heat dissipation, enhanced dispersion, and multimodal therapy potential [16–20]. However, conventional synthesis methods for TMDs/MNPs nanocomposites often require high temperatures and long processing times, as observed in the method developed by Ji Yu et al. [18].

This study presents an innovative, eco-friendly, and rapid approach for the synthesis of nanocomposites, utilizing the liquid-phase exfoliation (LPE) method, which is based on

ultrasonication, to exfoliate vdW in the presence of GA and MNPs. LPE eliminates the need for high-temperature processing, ensuring biocompatibility and environmental sustainability. Furthermore, this is the first study to report the application of MoSe<sub>2</sub> and TiS<sub>2</sub> in magnetic hyperthermia therapy, comparing their performance with that of graphene, WS<sub>2</sub>, and MoS<sub>2</sub>, where high stability, tunability, and environmental compatibility are crucial. By combining the unique properties of TMDs with the magnetic tunability of MNPs, this study advances the development of theranostic platforms, bridging sustainability, efficiency, and biomedical applicability. In addition, besides biomedical applications, the synthesized nanocomposites hold significant potential in other technological domains, including optoelectronics, catalysis, and energy storage [19-21]. For instance, MNPs/graphene nanocomposites have demonstrated high efficiency in lithium-ion batteries, highlighting their versatility in next-generation technologies [22]. This study, therefore, addresses this gap, offering a transformative contribution to nanotechnology and biomedicine.

## **2.Methodology**

### **2.1 Materials**

Ferric chloride hexahydrate 99 % (FeCl<sub>3</sub>.6H<sub>2</sub>O), ferrous sulfate heptahydrate 99.5% (FeSO<sub>4</sub>.7H<sub>2</sub>O), ferric nitrate nonahydrate 99% (Fe(NO<sub>3</sub>)<sub>3</sub>.9H<sub>2</sub>O), ammonium hydroxide 28% (NH<sub>4</sub>OH), hydrochloric acid 37% (HCl), nitric acid 65% (HNO<sub>3</sub>), acetone, gum arabic, graphite powder, titanium (IV) sulfide (TiS<sub>2</sub>) 99.9%, molybdenum (IV) sulfide (MoS<sub>2</sub>)99%, tungsten (IV) sulfide (WS<sub>2</sub>) 99%, molybdenum (IV) selenide (MoSe<sub>2</sub>)99% were purchased from Sigma Aldrich (São Paulo, Brazil), all reagents used were of analytical grade, Milli-Q water was used to prepare the solutions.

## 2.2 Synthesis of MNPs

MNPs were synthesized via the coprecipitation method in alkaline medium [23,24]. A 225 mL aqueous solution containing 0.15 mol of  $\text{Fe}^{3+}$  and 0.074 mol of  $\text{Fe}^{2+}$  was subjected to mechanical agitation. Subsequently, 1 mol of  $\text{NH}_4\text{OH}$  in 500 mL of ultrapure water, was added dropwise under continuous stirring. The system remained under agitation for one hour, after which the precipitate was magnetically separated and washed with ultrapure water until the pH reached neutrality. Then, a 1 mol.  $\text{L}^{-1}$   $\text{HNO}_3$  solution was added until the precipitate was completely covered and the system remained under stirring for 15 minutes. The precipitate was magnetically separated, and the supernatant was discarded. Following this step, 100 mL of a 1 mol.  $\text{L}^{-1}$   $\text{Fe}(\text{NO}_3)_3$  solution was added, and the mixture was heated to boiling under continuous stirring for 20 minutes. After cooling, the dispersion was magnetically separated, and the remaining material was washed three times with acetone. To obtain a stable magnetic colloid, aliquots of ultrapure water were added until a final volume of 100 mL was reached. The resulting colloidal dispersion was stored for further characterization and testing. The final mass concentration of the magnetic colloid was  $0.11\text{g. mL}^{-1}$ . A schematic representation of the synthesis process can be seen in Figure S1.

## 2.3 Obtaining of Graphene@GA@MNPs and TMDs@GA@MNPs nanocomposites

Graphene@GA@MNPs and TMDs@GA@MNPs were synthesized from graphite and transition metal dichalcogenide (TMD) powders, respectively, via ultrasonic liquid-phase exfoliation using water as the solvent. For Graphene@GA@MNPs, 0.1 g of gum arabic was dissolved in 9.1 mL of ultrapure water, and 0.9 mL of magnetic colloid was added to this solution, which was then mixed with 1 g of graphite previously placed in a test tube. For the TMDs@GA@MNPs samples, 0.02 g of gum arabic and 0.2 mL of magnetic

colloid were dissolved in 9.1 mL of ultrapure water and added to 0.05 g of the corresponding TMD powder ( $WS_2$ ,  $MoS_2$ ,  $TiS_2$ , or  $MoSe_2$ ) prepared individually. Each dispersion was subjected to sonication in an ultrasonic bath (Elma S60 Ultrasonic Cleaners (5.75 lit) 150W, Ultrasonic Frequency 37 kHz, origin Germany) for 4 hours on two consecutive days, a total of 8 hours, with the temperature maintained at 20 °C using a circulating water bath. After exfoliation, the dispersions were left to stand for 24 hours. The supernatant was then collected and centrifuged at 15,000 rpm for 20 minutes, after which the precipitate was discarded. The resulting supernatant, containing Graphene@GA@MNPs or TMDs@GA@MNPs, was stored for characterization and further applications. The composites in the presence of a magnet can be seen in Figure S2.

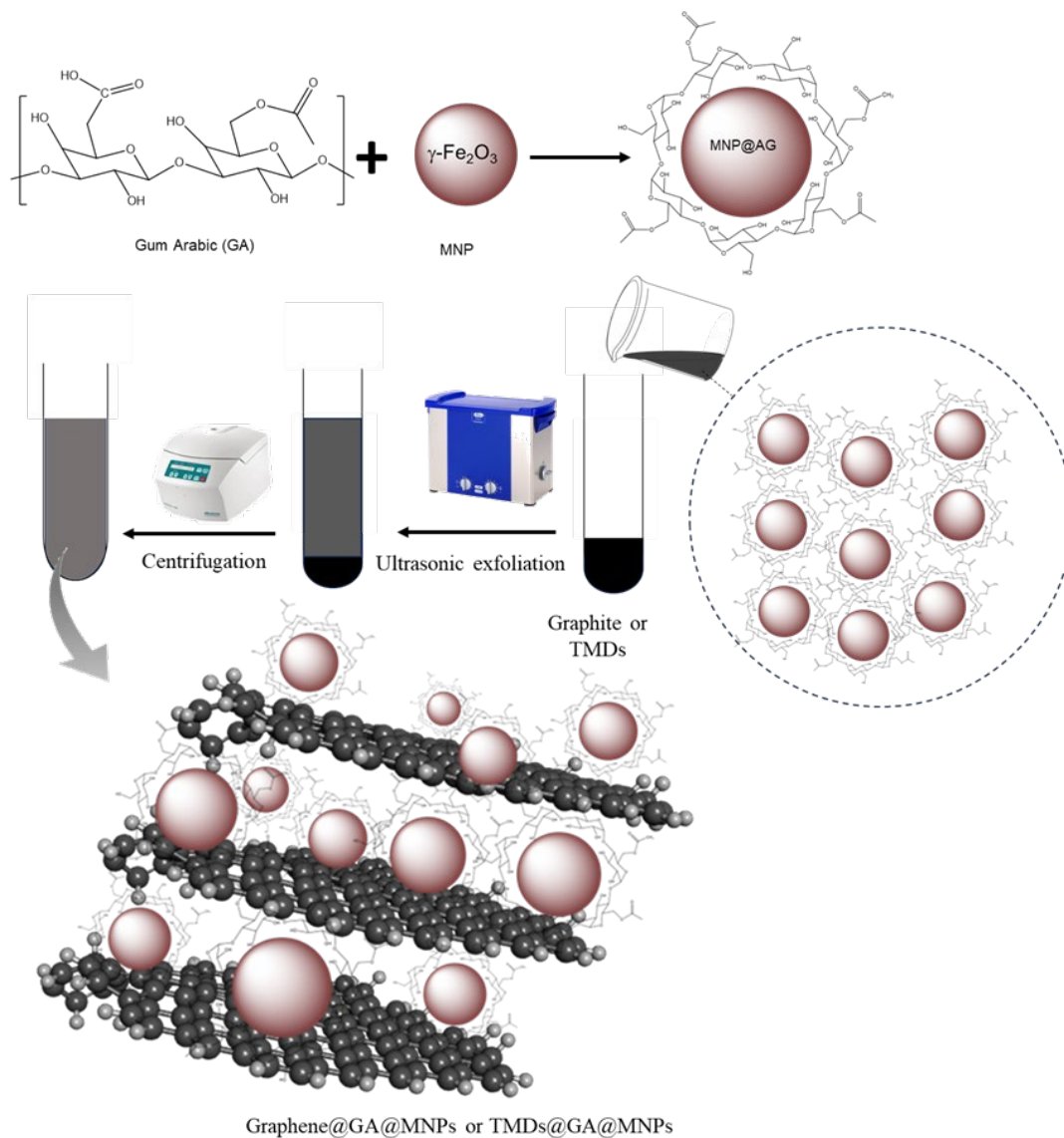


**Figure 1** – Schematic representation of nanocomposites preparation.

## 2.4 Characterization

Structural characterisation was obtained by X-ray powder diffraction (XRD) using a Panalytical Mpyrean diffractometer, with a copper tube, in a range scan between  $10^\circ$  and  $70^\circ$ , scan step 0.02 and velocity  $0.5^\circ/\text{min}$ . The morphology and size of nanostructures were determined by Transmission electron microscopy (TEM) imaging using a probe-corrected FEI Titan 80-300 TEM operating at 200 kV in the scanning TEM mode (STEM). The microscope is equipped with an Oxford Aztec Energy TEM Advanced

Microanalysis System for energy-dispersive spectroscopy (EDS) analysis. The samples were diluted tenfold in distilled water, sonicated for approximately 5 minutes, and a single drop was deposited onto a conventional 300-mesh Cu holey carbon TEM grid. The samples were studied by Raman spectroscopy using a Horiba LabRAM spectrometer with a 532 nm excitation laser, 5% power, 10 accumulations of 15 seconds, a 50× objective, and a diffraction grating of 1800 nm. The spectra were obtained at room temperature in the range of 200 to 2900  $\text{cm}^{-1}$ . FTIR measurements were conducted using a Bruker spectrophotometer model Vertex 70 in absorbance mode, employing potassium bromide (KBr) pellets. The spectra were obtained in the region from 4000  $\text{cm}^{-1}$  to 400  $\text{cm}^{-1}$  with a resolution set to 1  $\text{cm}^{-1}$  and 60 scans. Zeta potential ( $\zeta$ ) measurements as a function of pH were performed on a ZetaSizer Malvern Nano Series equipment (Model 3600), through Electrophoretic Light Scattering (ELS). An automatic MPT-2 autotitrator (Malvern Instruments) with NaOH and/or HNO<sub>3</sub> standard solutions were used to vary the pH of the dispersion. Thermogravimetric analysis (TGA) and thermal differential analysis (DTA) were performed using a Shimadzu DTG 60 equipment using nitrogen as a carrier gas. Samples were heated at a rate of 50°C/min and data were collected in the range of 42°C to 955°C. Magnetic measurements were conducted using a SQUID (Superconducting Quantum Interference Device) magnetometer, model MPMS 3, from Quantum Design. Hysteresis loops, as well as Zero Field Cooled (ZFC) and Field Cooled (FC) measurements, were carried out in the temperature range from 5 to 300 K, with an applied external field of  $H = 70$  Oe. For magnetic hyperthermia measurements a MagneTherm equipment from nanoTherics with a working frequency of 104.1 kHz, coil type 18T 44m, and capacitance of 200 nF. The sample was exposed to a magnetic field of 300 Oe for 4 minutes with a probe of the optical fiber.

### **3. Results and discussion**

#### **3.1 XRD investigation**

To confirm the production vdW nanocomposites and assess the role of MNPs in the exfoliation process, XRD measurements were conducted on the synthesized nanocomposites (Graphene@GA@MNPs and TMDs@GA@MNPs) to confirm the formation of Van der Waals nanocomposites and assess the role of MNPs in the exfoliation process. The diffraction patterns were compared with those of pure maghemite MNPs, bulk graphite (used as the starting material for exfoliation), and graphite exfoliated solely with GA (Graphene@GA). The resulting diffraction patterns for these samples are presented in Figure 2.

Figure 2 presents the XRD results for the synthesized magnetic nanocomposite (Graphene@GA@MNPs), along with its precursors — graphite and MNPs — for comparison, as well as graphene exfoliated using only GA. The diffractograms of Graphene@GA@MNPs and TMDs@GA@MNPs were compared with those of pure graphite, pure maghemite, and graphene obtained using only GA (Graphene@GA).

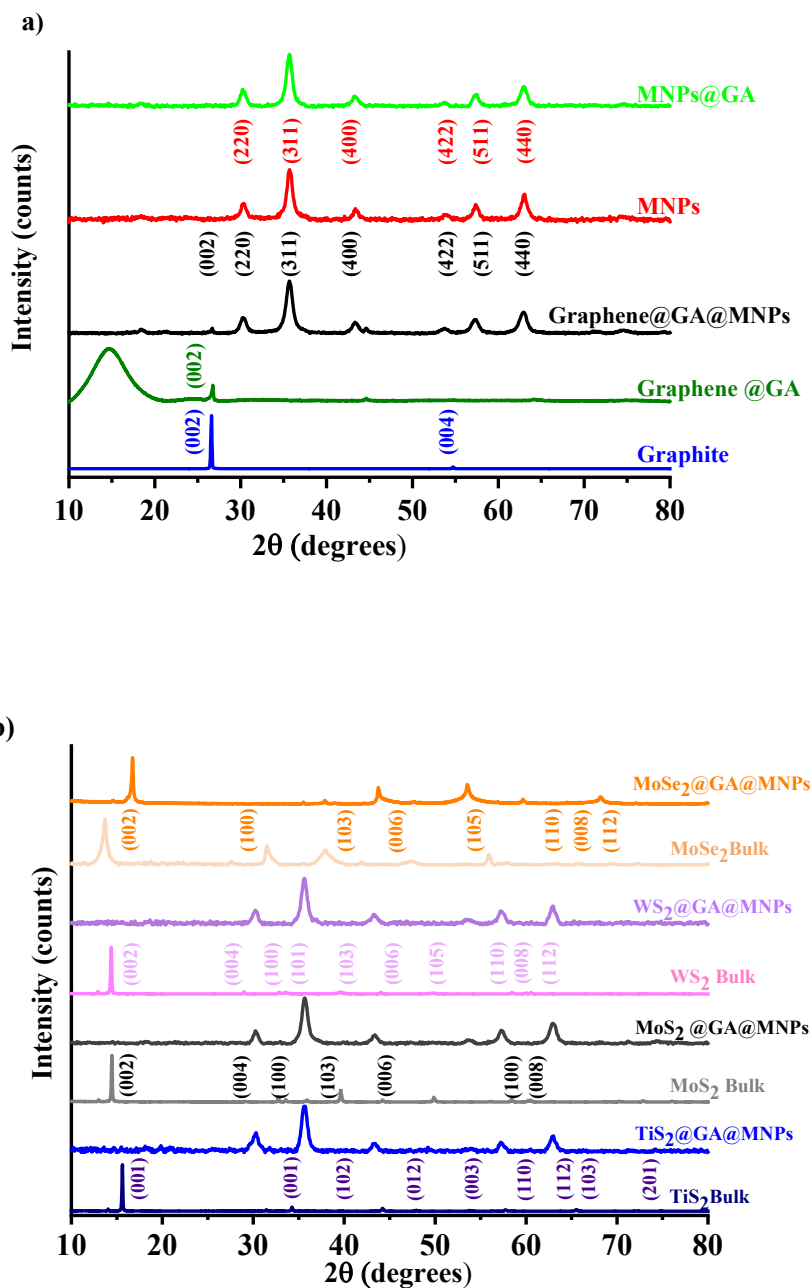


**Figure 2** – XRD diffractograms of (a) Graphene@GA@MNPs composites and (b) TMDs@GA@MNPs. The plots include the diffractograms of MNPs functionalized with GA, pure and MNPs. The Van der Waals materials exfoliated using only GA for comparative analysis are in material supplementary, Figure S3.

Graphite exhibited an intense (002) peak centered at 26.5°, corresponding to an interlayer spacing of 0.34 nm, along with the (004) reflection, characteristic of higher-order polyarene layer compounds. In the diffractogram of the MNPs (Figure 2a), the peaks

corresponding to the (220), (311), (422), (511), and (440) planes were assigned to maghemite ( $\gamma\text{-Fe}_2\text{O}_3$ ) based on the JCPDS 96-900-631 pattern [25-27]. The Graphene@GA sample showed a significant reduction in the (002) peak intensity, indicating a decrease in the number of layers, along with the appearance of an amorphous band at  $14.5^\circ$ , attributed to GA [28].

The Graphene@GA@MNPs (Figure 2a) samples showed a greater reduction in the intensity of the (002) plane and the absence of the (004) plane, confirming the formation of graphene with fewer layers. The shift in the (002) peak suggests structural defects such as stacking disorder and edge dislocations caused by the exfoliation process. The presence of maghemite diffraction peaks in the Graphene@GA@MNPs sample, along with the reduction in (002) plane intensity, indicates that MNPs assist in the exfoliation process by disrupting Van der Waals interactions and facilitating graphene formation. These results confirm the successful production of a magnetic nanocomposite.

XRD analysis was also performed to investigate the crystalline structure of magnetic nanocomposites formed by exfoliated TMDs ( $\text{WS}_2$ @GA@MNPs,  $\text{MoS}_2$ @GA@MNPs,  $\text{TiS}_2$ @GA@MNPs, and  $\text{MoSe}_2$ @GA@MNPs) in combination with GA and MNPs. The diffractograms of MNPs confirmed their high crystallinity, with characteristic peaks indicating that the presence of GA does not alter their crystalline structure, although it reduces the intensity of some reflections due to surface coverage. The diffractograms of the TMDs exfoliated using only gum arabic can be seen in Figure S3 (please, see supplementary material).

It is well established in the literature that the reduction in peak intensity of these planes is associated with a decrease in the number of layers, particularly in the (002) plane, as this reflection directly corresponds to layer stacking along the c-axis, which is most

affected by exfoliation [26,27]. For TMDs (Figure 2b), the diffractograms revealed a significant reduction in the intensity of the (002), (004), and (006) reflections in the exfoliated samples, indicating a decrease in the number of layers. This reduction was even more pronounced in the nanocomposites, attributed to structural disorder induced by exfoliation, the insertion of nanoparticles between layers, and surface coverage by GA. The presence of maghemite's characteristic diffraction peaks in all nanocomposites confirmed the successful incorporation of nanoparticles into the TMDs flakes, validating the formation of magnetic nanocomposites. These results are further supported by Figures S3 and S4, which show representative transmission electron microscopy (TEM) images of the synthesized and exfoliated materials. In these images, the coexistence of Van der Waals flakes and MNPs is evident. Additionally, regions with distinct intensities, particularly at the Van der Waals edges, suggest overlapping flakes and the formation of few-layer or multilayer Van der Waals structures intercalated with MNPs. Furthermore, the TEM images show that the lateral size of TMDs flakes are in the nanometric size range, whereas the graphene flakes are in the micrometer range. Scanning electron microscopy (SEM) images, EDS spectra, and EDS elemental mappings of the TMDs@GA@MNPs samples are presented in Figures S5–S9 and confirm the presence of elements corresponding to all components of the nanocomposites.

### **3.3 Raman analysis**

Raman spectroscopy is a powerful technique widely used to evaluate the quality of graphene and determine the number of layers [29,30]. Raman spectroscopy was used to evaluate the quality of the exfoliated materials and their interactions with GA and MNPs.

Figure 3 presents the Raman spectra of Van der Waals materials functionalized with GA, MNPs, and the powdered graphite used for exfoliation.

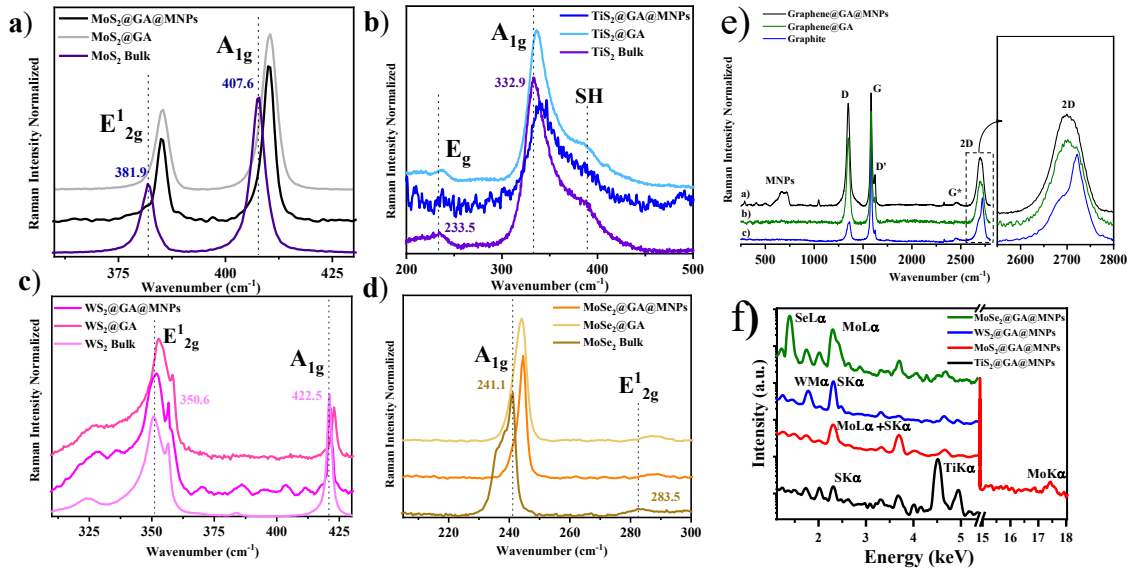


Figure 3 – Raman spectra of (a)  $\text{MoS}_2@GA@MNPs$ , (b)  $\text{TiS}_2@GA@MNPs$ , (c)  $\text{WS}_2@GA@MNPs$ , (d)  $\text{MoSe}_2@GA@MNPs$ , (e)  $\text{Graphene@GA@MNPs}$  nanocomposites, and (f) EDS spectra of the four TMDs samples, collected over an area of approximately 100 nm.

Each spectrum includes, for comparison, the Raman spectra of Van der Waals materials exfoliated using only GA. Additionally, a zoomed-in view of the region between  $2600\text{ cm}^{-1}$  and  $2800\text{ cm}^{-1}$  is shown on the right side of Figure 3e, highlighting the 2D band.

The spectrum in Figure 3e corresponds to the  $\text{Graphene@GA@MNPs}$  sample. The bands at  $220\text{ cm}^{-1}$ ,  $287\text{ cm}^{-1}$ ,  $408\text{ cm}^{-1}$ ,  $498\text{ cm}^{-1}$ ,  $664\text{ cm}^{-1}$ ,  $717\text{ cm}^{-1}$ , and  $1047\text{ cm}^{-1}$  are attributed to MNPs. The presence of maghemite bands confirms the formation of the magnetic nanocomposite, corroborated by XRD and TEM analyses.

Consistent with previous reports, exfoliated graphene exhibits characteristic Raman peaks at  $1340\text{ cm}^{-1}$ ,  $1582\text{ cm}^{-1}$ ,  $1623\text{ cm}^{-1}$ ,  $2456\text{ cm}^{-1}$ , and  $2702\text{ cm}^{-1}$ , corresponding to the D, G, D', G\*, and 2D bands, respectively [30,32]. The defect density in graphitic materials is typically estimated from the intensity ratio between the D and G bands ( $I_D/I_G$ ) [33], where a higher ratio indicates a greater defect density. The  $I_D/I_G$  ratios for graphite,  $\text{Graphene@GA}$ , and  $\text{Graphene@GA@MNPs}$  were 0.57, 0.76, and 0.90, respectively,

indicating that the obtained graphene has a higher defect density than graphite. This suggests an exfoliated structure with increased defects, particularly in samples containing nanoparticles. highlight the effectiveness of the liquid exfoliation methodology, with the interaction between MNPs and graphene evidenced by the 2D band shift. TEM and XRD analyses further confirm the successful production of few-layer graphene.

For the TMDs ( $\text{MoS}_2$ ,  $\text{TiS}_2$ ,  $\text{WS}_2$ , and  $\text{MoSe}_2$ ), the  $E^{1_{2g}}$  and  $A_{1g}$  vibrational modes exhibited characteristic shifts, reflecting structural modifications while maintaining their crystalline nature. Specifically, for  $\text{MoS}_2$ , these vibrational modes showed significant shifts. The  $E^{1_{2g}}$  mode experienced a blueshift to  $385.3 \text{ cm}^{-1}$  and  $385.1 \text{ cm}^{-1}$  in the  $\text{MoS}_2@GA$  and  $\text{MoS}_2@GA@MNPs$  samples, respectively, compared to bulk  $\text{MoS}_2$  ( $381.9 \text{ cm}^{-1}$ ). On the other hand, the  $A_{1g}$  mode showed a redshift to  $410.3 \text{ cm}^{-1}$  and  $410.2 \text{ cm}^{-1}$  in the same samples, compared to  $407.6 \text{ cm}^{-1}$  in bulk  $\text{MoS}_2$ . Additionally, the frequency difference between the  $E^{1_{2g}}$  and  $A_{1g}$  modes for  $\text{MoS}_2$  was measured to be  $25.2 \text{ cm}^{-1}$ , corresponding to a thickness of approximately 6 to 8 layers [35].

For  $\text{TiS}_2$  in its bulk form, three distinct vibrational bands were observed at  $233 \text{ cm}^{-1}$ ,  $332.6 \text{ cm}^{-1}$ , and  $382.6 \text{ cm}^{-1}$ , corresponding to  $E^{1_{2g}}$ ,  $A_{1g}$ , and SH modes, respectively. These modes represent in-plane vibrations, out-of-plane vibrations, and a mode of unknown origin [35,36]. The SH mode is associated with defects, and its shift can be used to estimate the number of layers. According to the method proposed by Scherrell, the ratio between the intensities of the  $A_{1g}$  and SH vibrational modes is inversely related to the number of layers [36]. By calculating this ratio, values of 2.15, 3.0, and 2.69 were obtained for bulk  $\text{TiS}_2$ ,  $\text{TiS}_2@GA$ , and  $\text{TiS}_2@GA@MNPs$ , respectively. These results suggest that both  $\text{TiS}_2@GA$  and  $\text{TiS}_2@GA@MNPs$  contain more than five layers, with greater exfoliation efficiency observed in samples without nanoparticles [35,36].

For WS<sub>2</sub>, the characteristic vibrational modes of the bulk sample appear at approximately 356 cm<sup>-1</sup> and 422 cm<sup>-1</sup>, corresponding to the E<sup>1</sup><sub>2g</sub> and A<sub>1g</sub> modes, respectively. Additionally, the A<sub>1g</sub> mode exhibits a blueshift as the number of layers increases, reflecting a lattice stiffening effect and an increase in the spacing between characteristic vibrational modes [37,38]. To determine the number of layers, the methodology proposed by Zhao can be applied, which involves calculating the frequency difference between the E<sup>1</sup><sub>2g</sub> and A<sub>1g</sub> modes [37]. The frequency differences were determined as 65.5 cm<sup>-1</sup>, 68.3 cm<sup>-1</sup>, and 69.2 cm<sup>-1</sup> for monolayer, bilayer, and trilayer samples, respectively. For samples with four or more layers, this difference converges to the bulk value of approximately 70 cm<sup>-1</sup>. For the bulk, WS<sub>2</sub>@GA, and WS<sub>2</sub>@GA@MNPs samples, the calculated frequency differences were 70.48 cm<sup>-1</sup>, 70.16 cm<sup>-1</sup>, and 70.0 cm<sup>-1</sup>, respectively. A slight reduction in the frequency difference compared to the bulk sample suggests that both WS<sub>2</sub>@GA and WS<sub>2</sub>@GA@MNPs contain more than four layers, regardless of the presence of magnetic nanoparticles.

For MoSe<sub>2</sub>, the characteristic vibrational modes appear at 241 cm<sup>-1</sup>, corresponding to the out-of-plane A<sub>1g</sub> mode, and at approximately 285.3 cm<sup>-1</sup>, corresponding to the in-plane E<sup>1</sup><sub>2g</sub> mode [39]. When comparing the MoSe<sub>2</sub>@GA@MNPs and MoSe<sub>2</sub>@GA samples with the bulk material, a shift in both vibrational modes is observed, indicating successful exfoliation. Specifically, for the A<sub>1g</sub> mode, Tondorf demonstrated that a redshift occurs with a decrease in the number of layers, with a 2 cm<sup>-1</sup> redshift observed when transitioning from bulk to monolayer MoSe<sub>2</sub> [40]. In the exfoliated samples, the shifts were 3 cm<sup>-1</sup> and 3.44 cm<sup>-1</sup> for the MoSe<sub>2</sub>@GA and MoSe<sub>2</sub>@GA@MNPs samples, respectively, suggesting that the obtained flakes contain fewer than 10 layers [40].

In all materials, interactions with GA and MNPs caused linewidth variations, indicating modifications in the structural environment. STEM-EDS analysis (figure 3f) revealed that

vdW materials in particles smaller than 5 nm are dispersed around the MNPs, with some particles reaching sizes of a few dozen nanometers. Refer to the EDS maps and STEM images (figures S5-S8) in the supplementary information for further details.

The bands attributed to MNPs further supported the formation of magnetic nanocomposites, corroborated by complementary TEM, EDS and XRD analyses. These results confirm the effectiveness of the liquid exfoliation method using GA and MNPs, demonstrating its efficiency and versatility in producing nanocomposites with tunable properties and enhanced potential for diverse technological applications.

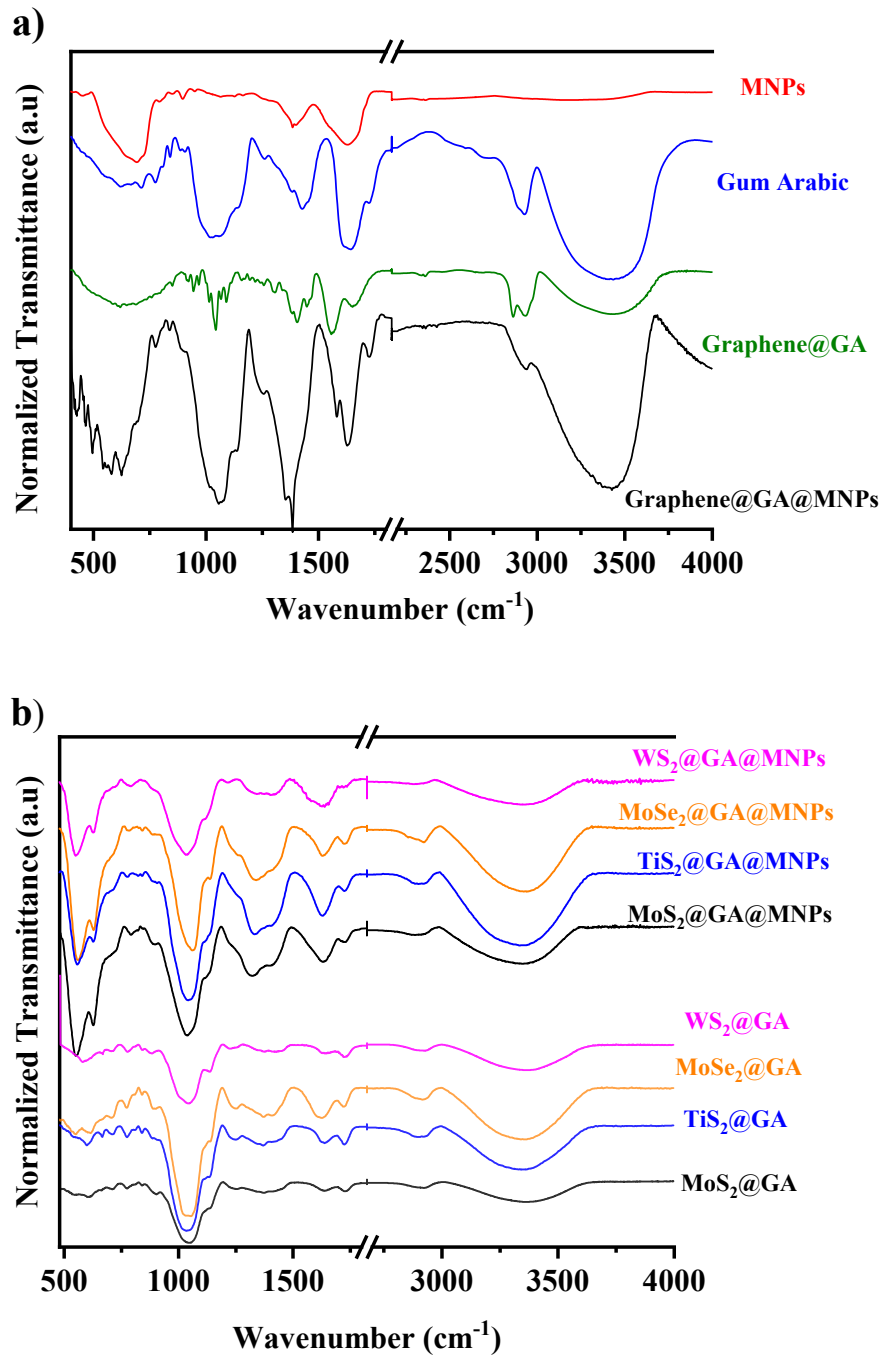
### **3.4 FT-IR study**

Figure 4 shows the infrared absorption spectra of GA, maghemite MNPs, graphene, and TMDs exfoliated using either GA alone or a combination of GA and maghemite nanoparticles. The FTIR spectrum of GA reveals characteristic functional groups, including carboxylates, hydroxyls, and amines, along with a fingerprint region (900–1050  $\text{cm}^{-1}$ ) attributed to C–O stretching in arabinogalactan chains. The band at 1400  $\text{cm}^{-1}$  and 1729  $\text{cm}^{-1}$  corresponds to C=O stretching, while the band at 1360  $\text{cm}^{-1}$  is assigned to O–H bending [41]. The broad absorption band in the 3400–3500  $\text{cm}^{-1}$  region corresponds to O–H stretching vibrations [42,43]. The band at 2926  $\text{cm}^{-1}$  indicates the presence of arabinose, associated with C–H stretching, while the band at 1264  $\text{cm}^{-1}$  corresponds to C–O stretching [44,45]. This spectral region was observed in all samples containing GA, with shifts and intensity variations due to interactions among the components.

The FTIR spectrum of MNPs exhibits a broad band at 3423  $\text{cm}^{-1}$  and 1627  $\text{cm}^{-1}$ , attributed to the stretching and bending vibrations of surface hydroxyl (O–H) groups, respectively. The peaks at 629  $\text{cm}^{-1}$ , 587  $\text{cm}^{-1}$ , and 560  $\text{cm}^{-1}$  correspond to Fe–O vibrational modes, confirming the presence of iron oxide [17,44,45].

In the Graphene@GA@MNPs and TMDs@GA@MNPs samples, the increased intensity of bands in the 400–700  $\text{cm}^{-1}$  region further confirmed the incorporation of nanoparticles into the nanocomposites. The interaction between the O–H and C=O groups of GA with Fe in the MNPs, along with Van der Waals and  $\pi$ – $\pi$  interactions in graphene, facilitated the exfoliation and stabilization of the nanocomposites [17]. For TMDs, these interactions are believed to be predominantly governed by Van der Waals forces due to the presence of acetyl groups.

In the Graphene@GA and Graphene@GA@MNPs samples, peaks associated with the G band (characteristic of  $\text{sp}^2$ -hybridized carbon) confirmed the production of graphene. Modifications in the spectrum, such as the disappearance of the C=O band and the appearance of bands related to C-H ( $\text{sp}^3$ ) bonds, indicate structural changes resulting from component interactions. The reduction in intensity and narrowing of the -OH band at 3400  $\text{cm}^{-1}$  in samples with MNPs further reinforce the interactions between arabic gum, nanoparticles, and the exfoliated material. These results confirm the formation and stabilization of magnetic nanocomposites.



**Figure 5** - FTIR spectra of (a) MNPs, Gum Arabic and Graphene@GA@MNPs and (b) TMDs@GA@MNPs nanocomposites. For comparison, each spectrum includes the FTIR data of vdW materials exfoliated using only GA.

### 3.5 Colloidal Stability

Figure 6 presents the zeta potential as a function of pH for the MNPs and composite samples. The MNPs exhibit a typical zeta potential profile in aqueous dispersion, consistent with previous reports on magnetic oxides [45]. The nanoparticle surface

behaves like a weak diprotic Brønsted acid. At acidic pH, a maximum positive zeta potential of +50 mV is observed at pH = 2.2, attributed to the presence of  $-\text{FeOH}_2^+$  groups. As the pH increases, deprotonation occurs, forming  $-\text{FeOH}$ , which leads to a decrease in surface charge, reaching a zero-zeta potential between pH 8 and 10. At basic pH, further deprotonation generates  $-\text{FeO}^-$  species, causing charge inversion and a negative zeta potential of  $-47.7$  mV at pH = 11.8.

In contrast, the Graphene@GA@MNPs sample exhibits a markedly different behavior. At acidic pH, it already has a negative zeta potential of  $-1.98$  mV at pH = 2.2, which becomes increasingly negative as pH rises, reaching a minimum of  $-32.4$  mV at pH = 9.8. Unlike MNPs, this sample does not exhibit a point of zero charge, as no charge inversion occurs. This shift in zeta potential behavior is due to the GA coating on the MNPs, where strong interactions between O–H and C=O groups and Fe atoms modify the surface charge properties, eliminating the previous acidic behavior. Additionally, interactions between acetyl ( $-\text{COCH}_3$ ) groups and the graphene surface orient the polar groups of GA toward the aqueous medium. As a result, the zeta potential follows the acid-base behavior of carboxyl ( $-\text{COOH}$ ) groups, where at low pH, protonation dominates ( $-\text{COOH}$ ), leading to a slightly negative charge. As the pH increases, deprotonation occurs ( $-\text{COOH} \leftrightarrow -\text{COO}^- + \text{H}^+$ ), generating  $-\text{COO}^-$  species responsible for the progressively negative zeta potential. Notably, the Graphene@GA@MNPs nanocomposite exhibits strong electrostatic repulsion from pH  $\geq 4$ , enhancing its colloidal stability and improving its applicability in aqueous dispersions.

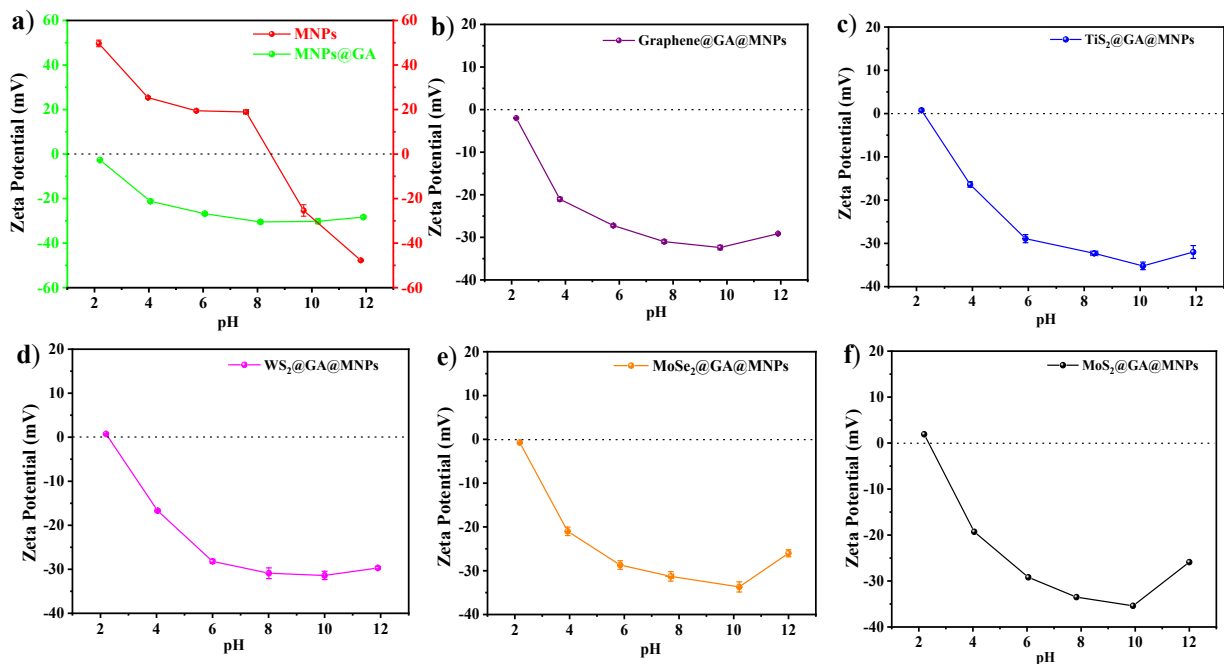


**Figure 6** – Zeta potential as a function of pH for (a) MNPs and MNPs@GA, (b) Graphene@GA@MNPs, (c) TiS<sub>2</sub>@GA@MNPs, (d) WS<sub>2</sub>@GA@MNPs, (e) MoSe<sub>2</sub>@GA@MNPs, and (f) MoS<sub>2</sub>@GA@MNPs samples.

The MNPs@GA sample (MNPs coated with GA, Figure 6a) exhibits distinct behavior compared to the uncoated MNPs (Figure 6a). The GA coating significantly shifts the zeta potential, imparting a predominantly negative surface charge across the entire pH range studied. At acidic pH (pH = 2.2), the zeta potential of MNPs@GA starts at approximately -10 mV, whereas uncoated MNPs exhibit positive values due to the presence of  $-\text{FeOH}_2^+$  groups. In the neutral to basic pH range, a gradual decrease in the zeta potential is observed, reaching a minimum of approximately -30 mV at basic pH, without charge inversion. This behavior is attributed to the  $-\text{COOH}$  groups in GA, which progressively deprotonate ( $-\text{COOH} \leftrightarrow -\text{COO}^- + \text{H}^+$ ) as pH increases, generating a predominant negative charge. The absence of a point of zero charge indicates that the GA coating masks the intrinsic acid-base behavior of MNPs, providing enhanced colloidal stability across a wide pH range, particularly under neutral and alkaline conditions.

A comparison between MNPs and MNPs@GA reveals fundamental differences. At acidic pH, MNPs exhibit a positive zeta potential (+50 mV) due to the protonation of  $-\text{FeOH}_2^+$  groups, whereas MNPs@GA already display a negative zeta potential (−10 mV), suggesting that the  $-\text{COOH}$  groups of GA are predominantly deprotonated. In the neutral to basic pH range, uncoated MNPs undergo charge inversion at pH 8–10, whereas MNPs@GA remain negatively charged throughout, indicating greater colloidal stability induced by GA. These differences highlight the impact of GA, which not only modifies the surface chemistry of MNPs but also enhances their dispersibility and stability in aqueous solutions.

The samples with GA combined with different TMDs ( $\text{MoSe}_2$ ,  $\text{WS}_2$ ,  $\text{MoS}_2$ , and  $\text{TiS}_2$ ) exhibit qualitatively similar behaviors. At acidic pH, the zeta potential of all samples remains slightly negative (−5 to −10 mV), indicating the presence of protonated  $-\text{COOH}$  groups. As pH increases, these  $-\text{COOH}$  groups progressively deprotonate, leading to more negative zeta potentials, reaching values between −30 and −40 mV at basic pH. All samples demonstrate high colloidal stability across a broad pH range due to the GA coating, which promotes strong electrostatic repulsion between particles. Despite the overall similarity in behavior, subtle differences in zeta potential values may arise from specific interactions between TMDs and GA, as well as variations in surface functionalization.

### **3.6 Magnetic properties**

The magnetic properties of the nanocomposites were investigated through magnetization versus applied field ( $M \times H$ ) measurements at 300 K and 5 K, along with field-cooled (FC) and zero-field-cooled (ZFC) curves. GA functioned as a stabilizer and dispersant, influencing the interactions between maghemite magnetic nanoparticles, graphene, and TMDs.

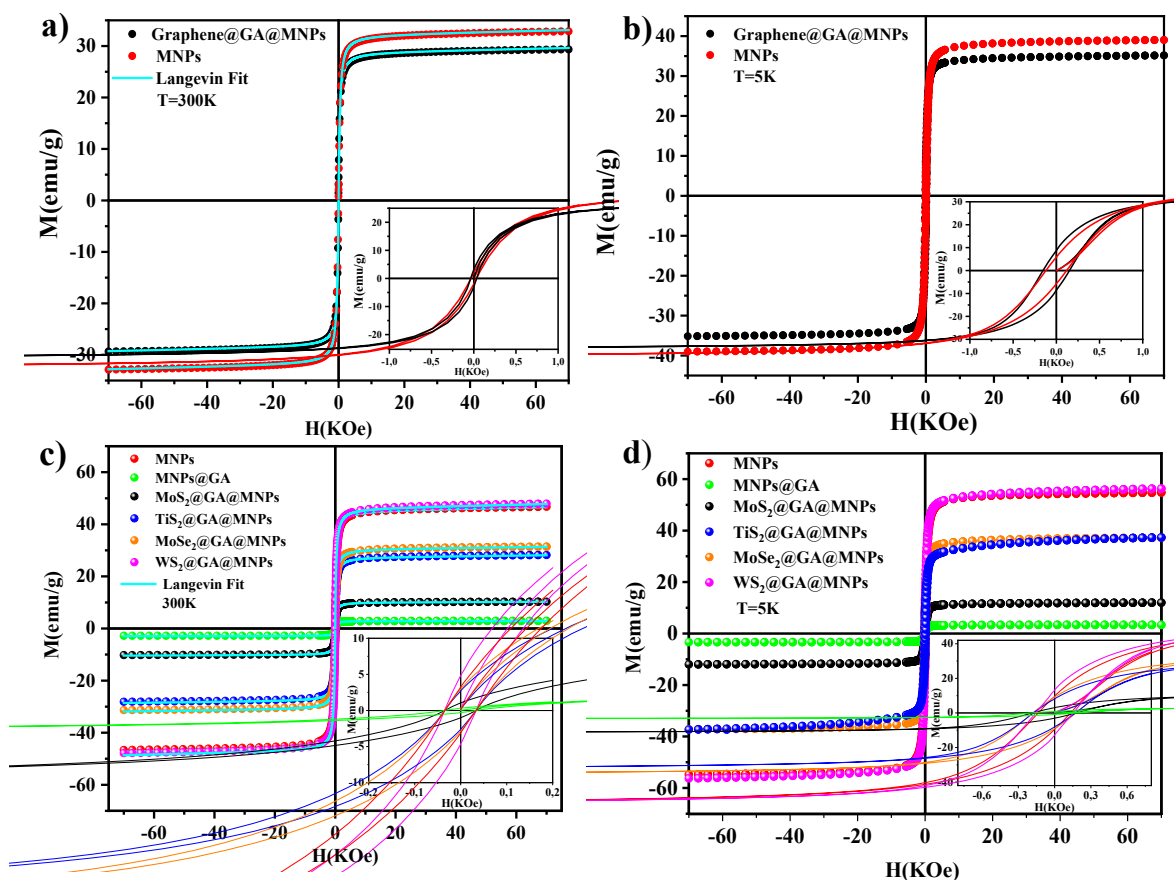


**Figure 8** –  $M \times H$  curves of the vdW nanocomposites at 300 K and 5 K. Panels (a) and (b) display the curves at 300 K and 5 K, respectively, for Graphene@GA@MNPs (black line) and MNPs (red line). Panels (c) and (d) show the curves at 300 K and 5 K for TMDs@GA@MNPs, MNPs@GA, and MNPs. The insets in each panel provide a magnified view of the central region at both temperatures. Additionally, the 300 K curves in panels (a) and (c) were fitted using the Langevin model to analyze the magnetic behavior.

The  $M \times H$  results indicate superparamagnetic behavior at 300 K, transitioning to ferromagnetic behavior at 5 K, as evidenced by the appearance of hysteresis loops, consistent with previous reports [46]. A reduction in saturation magnetization and an increase in coercivity were observed at both 300 K and 5 K, in agreement with literature findings [47]. Compared to MNPs, the nanocomposites exhibit a reduction in saturation magnetization, except for the  $WS_2@GA@MNPs$  sample, which shows a saturation magnetization approximately equal to that of the pure nanoparticles. Since saturation magnetization ( $M_s$ ) is directly proportional to the magnetic moment ( $\mu$ ) per unit volume,

this decrease is likely due to magnetic disorder caused by environmental alterations introduced by 2D materials and GA. These modifications may result in overlapping magnetization vectors from different magnetic domains, leading to competing interactions and, consequently, a reduction in the overall magnetic moment. Another possible explanation is that the magnetic nanoparticles are anchored to the surface of the 2D material flakes, which could further decrease saturation magnetization. This effect directly contributes to the observed reduction in saturation magnetization [48,49]. In our system, anisotropy likely arises from a combination of effects—including magnetocrystalline, surface, shape, and defect-induced contributions [50]. These are further modulated by interactions between the exfoliated vdW materials and the MNPs. These results confirm the successful formation of magnetic nanocomposites, consistent with XRD, TEM, and FTIR analyses.

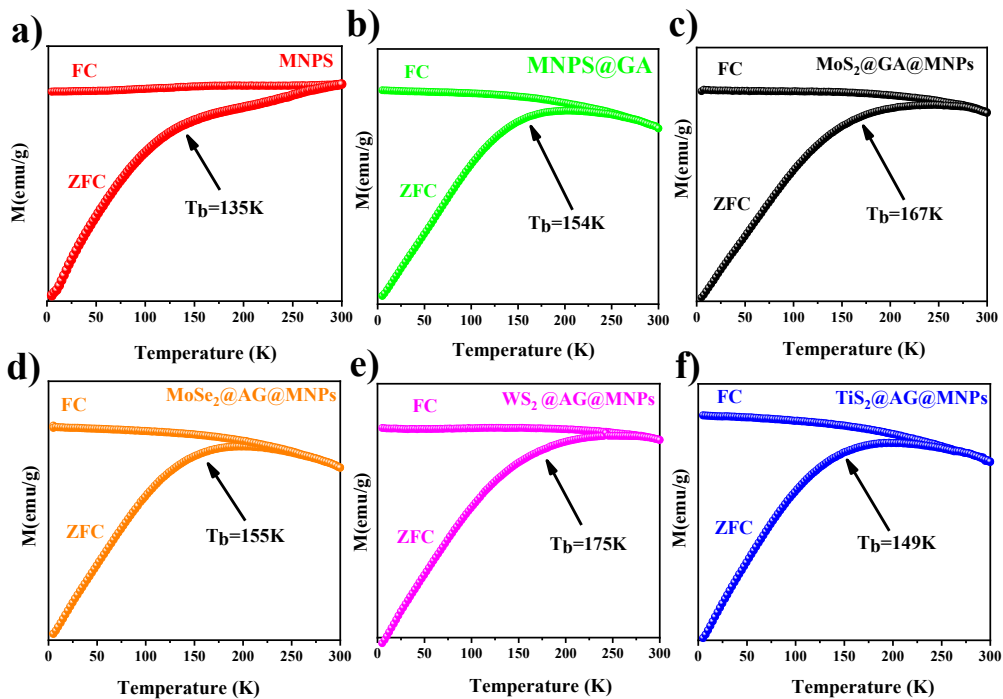


**Figure 9:** FC-ZFC curves of the nanocomposites: (a) Graphene@GA@MNPs, (b) MoS<sub>2</sub>@GA@MNPs, (c) MoSe<sub>2</sub>@GA@MNPs, (d) WS<sub>2</sub>@AG@MNPs, and (e) TiS<sub>2</sub>@AG@MNPs. Additionally, powdered maghemite nanoparticles (shown in red in

panel a) and Arabic gum with nanoparticles (represented in panel f) are included for comparison.

The FC-ZFC curves indicate superparamagnetic behavior in all samples, with blocking temperatures ( $T_b$ ) varying depending on the interaction between 2D materials and MNPs. The increase in  $T_b$  may be attributed to an increase in particle size and/or modifications in magnetic anisotropy induced by the presence of 2D materials. This further confirms the successful formation of the nanocomposite and suggests that the nanoparticles are anchored to the surface of the 2D material flakes. Additionally, the broadening of the peak in the ZFC curve suggests the presence of magnetic dipolar interactions among maghemite nanoparticles. These findings highlight the role of graphene, TMDs, and GA in tuning magnetic properties for specific applications.

### **3.7 Magnetic hyperthermia measurements**

MNPs can be functionalized with specific ligands to target them to cancer cells or tissues, allowing the delivery of anticancer drugs or imaging contrast agents, thereby reducing side effects in healthy tissues. They are commonly composed of iron oxide, which can generate heat when exposed to an alternating magnetic field [49]. This is exploited in the technique of magnetic hyperthermia, where nanoparticles are directed to cancerous tissues and heated to typically above 42 °C [49]. This heat can be used to selectively destroy cancer cells or make them more sensitive to radiotherapy and chemotherapy. Therefore, we conducted magnetic hyperthermia measurements with the Graphene@GA@MNPs and TMDs@GA@MNPs samples to assess its heating potential and viability for this application. For these measurements, we used a concentration of 5 mg/mL of MNPs for Graphene@GA@MNPs, and concentrations of 4.54 mg/mL, 4.71 mg/mL, 2.00 mg/mL, and 2.15 mg/mL for MoS<sub>2</sub>@GA@MNPs, WS<sub>2</sub>@GA@MNPs,

TiS<sub>2</sub>@GA@MNPs, and MoSe<sub>2</sub>@GA@MNPs, respectively. The temperature profiles as a function of time for these samples are shown in Figure 10.

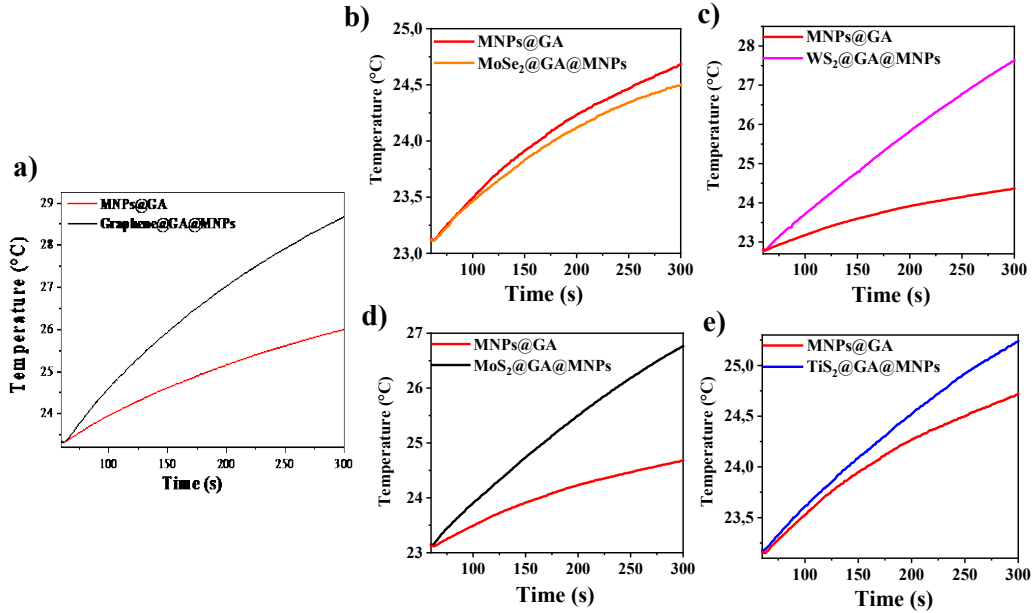


**Figure 10:** Heating rate measurements under a magnetic field applied for 4 minutes at 104.1 kHz and 300 Oe, for the following samples: (a) Graphene@GA@MNPs ( $C = 2.63$  mg/mL), (b) MoSe<sub>2</sub>@GA@MNPs ( $C = 2.15$  mg/mL), (c) WS<sub>2</sub>@GA@MNPs ( $C = 4.71$  mg/mL), (d) MoS<sub>2</sub>@GA@MNPs ( $C = 4.54$  mg/mL), and (e) TiS<sub>2</sub>@GA@MNPs ( $C = 2.00$  mg/mL).

A parameter used to determine the efficiency of a material in magnetic hyperthermia applications is the specific absorption rate (SAR), which is a rate expressed in watts per gram at which MNPs convert magnetic energy into heat [51]. This parameter directly depends on the thermal capacity of the nanocomposite and the magnetic mass of the nanoparticle in the sample [49]. The data necessary for calculating SAR was provided to the Nanotherics software during the measurement, and this parameter was obtained for the MNPs, Graphene@GA@MNPs and TMDs@GA@MNPs samples. The SAR value can be determined by equation [1]:

$$\text{SAR} = C (m_{\text{sol}}/m_{\text{MNPs}})(\Delta T/\Delta t). \quad (1)$$

Where  $C$  is heat capacity,  $(m_{\text{MNPs}})$  corresponds to the mass of the nanoparticles,  $(m_{\text{sol}})$  refers to the mass of the solvent, and the temperature gradient over time  $(\Delta T/\Delta t)$  [53]. In order to evaluate applicability and compare SAR values obtained from existing literature under different extrinsic conditions including magnetic field, frequency, size, and concentration of MNPs, the more suitable term to use is intrinsic loss power (ILP, in  $\text{nHm}^2\text{kg}^{-1}$ ) [53].

$$\text{ILP} [\text{nHm}^2\text{kg}^{-1}] = \text{SAR} / fH^2$$

The values of the SAR and ILP were obtained and can be seen in table 1:

**Table 1:** SAR values obtained for the Van der Waals materials in this study at a frequency of 105 kHz and an applied magnetic field of 24 kA/m.

<b>Material</b>	<b>SAR (W/g)</b>	<b>ILP (<math>\text{nHm}^2\text{kg}^{-1}</math>)</b>
Graphene@GA@MNPs	20.8	0.34
WS <sub>2</sub> @GA@MNPs	16.6	0.27
TiS <sub>2</sub> @GA@MNPs	23.3	0.38
MoS <sub>2</sub> @GA@MNPs	11.7	0.19
MoSe <sub>2</sub> @GA@MNPs	14.8	0.24
MNPs@GA	17.6	0.29

All nanocomposites developed in this study exhibited SAR values within the same order of magnitude, ranging from 11.7 to 23.3 W/g under identical experimental conditions (105 kHz and 24 kA/m), ensuring a fair comparison across samples. To further highlight the significance of our findings, we compared the SAR values of our nanocomposites with those reported in the literature. For example, for diverse metal ferrites, El-Boubbou et al. [54] reported SARs like 23.0 W/g for PVP-CoFe<sub>2</sub>O<sub>4</sub>, 39.0 W/g for PVP-NiFe<sub>2</sub>O<sub>4</sub>, 25W/g for PVP-ZnFe<sub>2</sub>O<sub>4</sub> and 14 W/g for PVP-MgFe<sub>2</sub>O<sub>4</sub> values while advanced Fe<sub>3</sub>O<sub>4</sub>

nanoparticles reported by Mohammadi et al. [55] achieved up to 14.8. Other studies, including Jalili et al. [56] reported SARs ranging from 21.0 W/g and 37.0 W/g to (CoFe<sub>2</sub>O<sub>4</sub>/Fe<sub>3</sub>O<sub>4</sub>) and (Fe<sub>3</sub>O<sub>4</sub>/CoFe<sub>2</sub>O<sub>4</sub>) nanocomposites, respectively, and Adhistinka et al. [53] reported 2.5 W/g for Fe<sub>3</sub>O<sub>4</sub>/CDs nanoparticles. Our Graphene@GA@MNPs, WS<sub>2</sub>@GA@MNPs, and TiS<sub>2</sub>@GA@MNPs samples exhibited SARs between 20.0 - 23.5 W/g.

All nanocomposites developed in this study exhibited SAR values within the same order of magnitude, ranging from 11.7 to 23.3 W/g under identical experimental conditions (105 kHz and 24 kA/m), ensuring a fair comparison across samples. Notably, the incorporation of magnetic nanoparticle and GA into the 2D materials matrix led to a significant enhancement in heating efficiency when compared to pure magnetic nanoparticles. For example, MNPs@GA alone showed a SAR of 17.6 W/g, while its corresponding nanocomposites such as TiS<sub>2</sub>@GA@MNPs and Graphene@GA@MNPs reached 23.3 W/g and 20.8 W/g, respectively. Notably, this is the first study to employ TiS<sub>2</sub> and MoSe<sub>2</sub> in magnetic hyperthermia, with TiS<sub>2</sub> showing particularly high efficiency. Furthermore, our WS<sub>2</sub>@GA@MNPs and MoS<sub>2</sub>@GA@MNPs nanocomposites are distinguished from previously reported systems using a different crystalline phase of the magnetic nanoparticles, contributing to their enhanced thermal performance. These results underscore the effectiveness of our green synthesis method using gum Arabic and the synergistic role of vdW materials in enhancing thermal response, positioning our system among the most promising candidates for biomedical hyperthermia.

The MNPs solely the value SAR found is higher than reported in [57,58]. Therefore, the presence of graphene and TMDs, which lack magnetic properties, increases the proportion of non-magnetic material, affecting the orientation of magnetic domains and

reducing the difficulty of alignment of magnetic moments, consequently improving heating efficiency [58]. In addition to the fact that nanoparticles exhibit a superparamagnetic character, leading to an increase in magnetic anisotropy, it is well known that magnetic interactions between nanoparticles strongly influence SAR [51,59].

For TMDs samples the SAR values indicated that higher concentrations of iron ions increase the energy dissipation capacity. Nanocomposites like  $\text{TiS}_2@\text{GA}@\text{MNPs}$ , which exhibited the highest SAR, on the other hand, materials like  $\text{MoSe}_2@\text{GA}@\text{MNPs}$  showed lower thermal efficiency, indicating weaker magnetic coupling.

The results indicate significant variations in the thermal properties of the nanocomposites, depending on the interactions between the nanoparticles, the applied magnetic field, and the individual characteristics of the TMDs. According to Olivia and her colleagues, increasing the thickness of the magnetically inert layer can influence the anisotropy of nanoparticles and promote more efficient heating of MNPs [51]. This increase affects the distribution of the magnetic field around the particle, altering the preferential orientation of magnetic domains within the nanoparticle and resulting in a more pronounced magnetic anisotropy, where the magnetic domains tend to align more strongly in a specific direction [57]. Additionally, a thicker inert layer can influence the particle's ability to respond rapidly to changes in the magnetic field, impacting heating efficiency and contributing to a more effective response of MNPs to alternating magnetic fields, thereby generating more heat.

Mehdaoui et al. have shown that the presence of magnetic interactions between MNPs reduces SAR [59]. We believe that the increase in SAR for the obtained nanocomposite is directly related to the presence of graphene and TMDs in the medium, which reduces the formation of aggregates, thereby decreasing the magnetic interactions between MNPs,

which corroborates with the previously obtained magnetic analyses. Thus, graphene and TMDs can play a significant role in modulating the magnetic properties of MNPs, such as magnetic anisotropy and heating efficiency in response to an alternating magnetic field, it plays an important role in rapidly dissipating heat during the heating process of MNPs.

The works that present Van der Waals materials for magnetic hyperthermia applications, and we achieved here was something never reported in the literature, which was the use of graphene or TMDs for magnetic hyperthermia applications using arabic gum, a surfactant which present high biocompatibility. This was made possible by using GA in the exfoliation process (a green exfoliation process), which promotes interaction with MNPs and simultaneously with the obtained graphene and TMDs, forming the nanocomposites.

Considering that the SAR is higher for the Graphene@GA@MNPs sample due to the presence of graphene which exhibits high specific heat capacity, and high thermal conductivity, reaches higher temperatures more quickly, we conclude that our magnetic nanocomposite Graphene@GA@MNPs and TMDs@GA@MNPs can be an excellent candidates for applications in the field of magnetic hyperthermia.

## **CONCLUSIONS**

This study successfully demonstrated the synthesis of novel vdW nanocomposites incorporating maghemite nanoparticles MNPs and GA as a stabilizing and exfoliation agent. The integration of WS<sub>2</sub>, MoS<sub>2</sub>, MoSe<sub>2</sub>, TiS<sub>2</sub>, and graphene into these nanocomposites not only optimized their magnetic and colloidal stability but also enabled precise control over their structural and thermal properties. The findings confirm that the interaction between MNPs and vdW materials plays a crucial role in modifying magnetic anisotropy and dipolar interactions, leading to a shifted blocking temperature and a

superparamagnetic response at 300 K. Additionally, the strong electrostatic repulsion (zeta potential  $\sim -30$  mV at  $\text{pH} \geq 4$ ) ensures long-term colloidal stability, a key requirement for biomedical applications. Magnetic hyperthermia tests demonstrated that Graphene@GA@MNPs and  $\text{TiS}_2$ @GA@MNPs achieved the highest specific absorption rates (SAR) of 21.4 W/g and 23.3W/g, respectively, under alternating magnetic fields. These values exceed those reported in the literature, reinforcing their potential for highly efficient heat generation in hyperthermia applications. Furthermore, the ability to magnetically guide these nanocomposites using external fields could enable targeted localized hyperthermia treatments, minimizing off-target effects and enhancing therapeutic precision. Overall, these results pave the way for next-generation multifunctional nanocomposites, bridging the gap between fundamental research and biomedical applications. Future studies could explore their biocompatibility, in vitro/in vivo performance, and long-term stability to further validate their potential for clinical use.

#### **Credit authorship contribution statement**

**J. Caland:** Investigation, writing – review & editing, Data curation. **A. Silva:** Investigation, writing – review & editing, Data curation. **J.Marroquin:** Investigation. **M. H. Sousa:** Investigation, writing – review & editing, Funding acquisition and Data curation **B. S. Archanjo:** writing – review & editing, Data curation. **P. Karagiannidis:** Investigation, writing – review & editing. **Jorlandio F. Felix:** Conceptualization, Data curation, Formal analysis, Funding acquisition, Investigation, Methodology, Project administration, Resources, Supervision, Validation, Writing – review & editing.

#### **Declaration of Competing Interest**

The authors declare that they have no known competing financial interests or personal relationships that could have appeared to influence the work reported in this paper.

#### **Data availability**

Data will be made available upon request.

## Acknowledgement

The authors acknowledge financial support from: CNPq (grant number: 309610/2021-4 and 315627/2021-2), Fundação de Apoio à Pesquisa do Distrito Federal (FAPDF, grant number: 193.00001823/2022-10, 00193-00002418/2023-08,00193-00000767/2021-15, 00193-00001264/2021-67 and 0193.00002588/2022-01).

## REFERENCES

- [1] A.K. Geim, I.V. Grigorieva, Van der Waals heterostructures, *Nature* 499 (2013) 419–425. <https://doi.org/10.1038/nature12385>.
- [2] S. Manzeli, D. Ovchinnikov, D. Pasquier, O. Yazyev, A. Kis, 2D Transition Metal Dichalcogenides, *Nat. Rev. Mater.* 2 (2017).<https://doi.org/10.1038/natrevmats.2017.33>.
- [3] D. Nutting, J. Felix, E. Tillotson, D.-W. Shin, A. De Sanctis, H. Chang, N. Cole, S. Russo, A. Woodgate, I. Leontis, H. Fernandez, M. Craciun, S. Haigh, F. Withers, Heterostructures formed through abraded Van der Waals materials, *Nat. Commun.* 11 (2020).<https://doi.org/10.1038/s41467-020-16717-4>.
- [4] S. Joseph, J. Mohan, S. Lakshmy, S. Thomas, B. Chakraborty, S. Thomas, N. Kalarikkal, A review of the synthesis, properties, and applications of 2D transition metal dichalcogenides and their heterostructures, *Mater. Chem. Phys.* 297 (2023) 127332.<https://doi.org/10.1016/j.matchemphys.2023.127332>.
- [5] J. Song, J. Zhang, K. Zheng, Z. Xu, K. Qi, Development process of graphene field for photocatalytic and antibacterial applications, *Desalin. Water Treat.* 297 (2023) 117-130.<https://doi.org/10.5004/dwt.2023.29592>.
- [6] P.G. Karagiannidis, S.A. Hodge, L. Lombardi, et al., Microfluidization of graphite and formulation of graphene-based conductive inks, *ACS Nano* 11 (2017) 2742-2755.<https://doi.org/10.1021/acsnano.6b07735>.
- [7] J. Chen, C. Liu, D. Hu, F. Wang, H. Wu, X. Gong, X. Liu, L. Song, Z. Sheng, H. Zheng, Single-Layer MoS<sub>2</sub> nanosheets with amplified photoacoustic effect for highly sensitive photoacoustic imaging of orthotopic brain tumors, *Adv. Funct. Mater.* 26 (2016) 8715–8725. <https://doi.org/10.1002/adfm.201603758>.

- [8] J. Shen, J. Liu, X. Fan, H. Liu, Y. Bao, A. Hui, H.A. Munir, Unveiling the antibacterial strategies and mechanisms of MoS<sub>2</sub>: A comprehensive analysis and future directions, *Biomater. Sci.* 12 (2024) 596-620. <https://doi.org/10.1039/D3BM01030A>.
- [9] Y. Zhao, H. Lee, W. Choi, W. Fei, C.J. Lee, Large-area synthesis of monolayer MoSe<sub>2</sub> films on SiO<sub>2</sub>/Si substrates by atmospheric pressure chemical vapor deposition, *RSC Adv.* 7 (2017) 27969–27973. <https://doi.org/10.1039/C7RA03642F>.
- [10] A. Kuc, N. Zibouche, T. Heine, Influence of quantum confinement on the electronic structure of the transition metal sulfide TiS<sub>2</sub>, *Phys. Rev. B* 83 (2011) 245213. <https://doi.org/10.1103/PhysRevB.83.245213>.
- [11] B. Fadee, J. Baker, L. Ballerini, C. Bussy, F. Candotto Carniel, M. Tretiach, M. Pelin, T. Buerki-Thurnherr, T. Kanerva, J.M. Navas, E. Vázquez, V. Rodriguez Unamuno, P. Lehtonen, M. González, H. Rauscher, J. Riego Sintes, K. Kostarelos, A. Bianco, M. Prato, Safety Assessment of Graphene-Based Materials, *Small* 21 (2025) 2404570. <https://doi.org/10.1002/sml.202404570>.
- [12] Xiaoling Ren, Peng Geng, Qin Jiang, Qian Ren, Daniel K. Macharia, Nuo Yu, Zhigang Chen, Synthesis of degradable titanium disulfide nanoplates for photothermal ablation of tumors, *Materials Today Advances* 14 (2022) 100241, ISSN 2590-0498, <https://doi.org/10.1016/j.mtadv.2022.100241>.
- [13] P.J. Sugumaran, X.L. Liu, T.S. Heng, E. Peng, J. Ding, GO-functionalized large magnetic iron oxide nanoparticles with enhanced colloidal stability and hyperthermia performance, *ACS Appl. Mater. Interfaces* 11 (2019) 22703-22713. <https://doi.org/10.1021/acsami.9b04261>.
- [14] F. Silva, H.P. Chang, J. Currivan-Incorvia, et al., 2D Nanomaterials and their drug conjugates for phototherapy and magnetic hyperthermia therapy of cancer and infections, *Small* 20 (2023). <https://doi.org/10.1002/sml.202306137>.
- [15] S. Wang, H. He, Y. Mao, Y. Zhang, N. Gu, Advances in atherosclerosis theranostics harnessing iron oxide-based nanoparticles, *Adv. Sci.* 11 (2024) 2308298. <https://doi.org/10.1002/advs.202308298>.

- [16] C.A. Quinto, P. Mohindra, S. Tong, G. Bao, Multifunctional superparamagnetic iron oxide nanoparticles for combined chemotherapy and hyperthermia cancer treatment, *Nanoscale* 7 (2015) 12728–12736. <https://doi.org/10.1039/C5NR03441F>.
- [17] Y. Yuan, B. Chen, L. Song, X. An, Q. Zhang, H. Lu, C.M. Li, C. Guo, Magnetic two-dimensional nanocomposites for multimodal antitumor therapy: A recent review, *J. Mater. Chem. B* 12 (2024) 1404–1428. <https://doi.org/10.1039/d3tb02333h>.
- [18] J. Yu, W. Yin, X. Zheng, G. Tian, X. Zhang, T. Bao, X. Dong, Z. Wang, Z. Gu, X. Ma, Y. Zhao, Smart MoS<sub>2</sub>/Fe<sub>3</sub>O<sub>4</sub> nanotheranostic for magnetically targeted photothermal therapy guided by magnetic resonance/photoacoustic imaging, *Theranostics* 5 (2015) 931–945. <https://doi.org/10.7150/thno.11802>.
- [19] S. Behrens, I. Appel, Magnetic nanocomposites, *Curr. Opin. Biotechnol.* 39 (2016) 89–96. <https://doi.org/10.1016/j.copbio.2016.02.005>.
- [20] I. Ismail, R.S. Azis, A review of magnetic nanocomposites for EMI shielding: synthesis, properties, and mechanisms, *J. Mater. Sci.* 59 (2024) 5293–5329. <https://doi.org/10.1007/s10853-024-09527-2>.
- [21] A. Jazzar, H. Alamri, Y. Malajati, R. Mahfouz, M. Bouhrara, A. Fihri, Recent advances in the synthesis and applications of magnetic polymer nanocomposites, *J. Ind. Eng. Chem.* 99 (2021) 1–18. <https://doi.org/10.1016/j.jiec.2021.04.011>.
- [22] O. Gerber, S. Bégin-Colin, B.P. Pichon, É. Barraud, S. Lemonnier, C. Pham-Huu, B. Daffos, P. Simon, J. Come, D. Bégin, Design of Fe<sub>3-x</sub>O<sub>4</sub> raspberry decorated graphene nanocomposites with high performances in lithium-ion batteries, *J. Energy Chem.* 25 (2016) 272–277. <https://doi.org/10.1016/j.jechem.2016.01.021>.
- [23] R. Massart, "Preparation of aqueous magnetic liquids in alkaline and acidic media," in *IEEE Transactions on Magnetics*, vol. 17, no. 2, pp. 1247–1248, March (1981), <https://doi.org/10.1109/TMAG.1981.1061188> .
- [24] A.O. Silva, A.F.C. Campos, M.O. Rodrigues, M.H. Sousa, Tuning magnetic and luminescent properties of iron oxide@C nanoparticles from hydrothermal synthesis: influence of precursor reagents, *Surf. Interfaces* 36 (2023) 101689, <https://doi.org/10.1016/j.surfin.2022.102624>.

- [25] C. Pecharromán, T. González-Carreño, J.E. Iglesias, The infrared dielectric properties of maghemite ( $\gamma\text{-Fe}_2\text{O}_3$ ) from reflectance measurement on pressed powders, *Phys. Chem. Miner.* 22 (1995) 21-29. <https://doi.org/10.1007/BF00202677>.
- [26] M. Zulfiqar, M. Rahman, M. Usman, et al., Static magnetic properties of maghemite nanoparticles, *J. Korean Phys. Soc.* 55 (2014) 1299-1303. <https://doi.org/10.3938/jkps.65.1925>.
- [27] H. Park, N. Myung, H. Jung, H. Choi, As(V) remediation using electrochemically synthesized maghemite nanoparticles, *J. Nanopart. Res.* 11 (2009) 1981-1989. <https://doi.org/10.1007/s11051-008-9558-x>.
- [28] M. Mir, S. Haripriya, Assessment of physical and structural characteristics of almond gum, *Int. J. Biol. Macromol.* 93 (2016) 10-20. <https://doi.org/10.1016/j.ijbiomac.2016.09.009>.
- [29] A.C. Ferrari, J.C. Meyer, V. Scardaci, et al., Raman spectrum of graphene and graphene layers, *Phys. Rev. Lett.* 97 (2006) 187401. <https://doi.org/10.1103/PhysRevLett.97.187401>.
- [30] D. Yoon, H. Moon, H. Cheong, et al., Variations in the Raman spectrum as a function of the number of graphene layers, *J. Korean Phys. Soc.* 55 (2009) 1299-1304.
- [31] T. Shimada, T. Sugai, C. Fantini, et al., Raman spectroscopy of graphene oxide, *Carbon* 43 (2005) 1049-1054. <https://doi.org/10.1016/j.carbon.2004.11.044>.
- [32] D. Graf, F. Molitor, K. Ensslin, C. Stampfer, A. Jungen, C. Hierold, L. Wirtz, Raman imaging of graphene, *Solid State Commun.* 143 (2007) 44-46. <https://doi.org/10.1016/j.ssc.2007.01.050>.
- [33] Z. Ni, Y. Wang, T. Yu, Z. Shen, Raman spectroscopy and imaging of graphene, *Nano Res.* 1 (2008) 273-291. <https://doi.org/10.1007/s12274-008-8036-1>.
- [34] C. Lee, H. Yan, L.E. Brus, T.F. Heinz, J. Hone, S. Ryu, Anomalous lattice vibrations of single- and few-layer  $\text{MoS}_2$ , *ACS Nano* 4 (2010) 2695-2700. <https://doi.org/10.1021/nn1003937>

- [35] J. Wu, W. Zhong, C. Yang, W. Xu, R. Zhao, H. Xiang, Q. Zhang, X. Li, N. Yang, Sulfur-vacancy rich nonstoichiometric  $\text{TiS}_{x-2}$  nanostructures for superior universal hydrogen evolution, *Appl. Catal. B Environ.* 310 (2022) 121332. <https://doi.org/10.1016/j.apcatb.2022.121332>
- [36] P.C. Sherrell, K. Sharda, C. Grotta, et al., Thickness-dependent characterization of chemically exfoliated  $\text{TiS}_2$  nanosheets, *ACS Omega* 3 (2018) 8655–8662. <https://doi.org/10.1021/acsomega.8b00766>.
- [37] W. Zhao, Z. Ghorannevis, K. Amara, et al., Lattice dynamics in mono- and few-layer sheets of  $\text{WS}_2$  and  $\text{WSe}_2$ , *Nanoscale* 5 (2013) 9677–9683. <https://doi.org/10.1039/C3NR03052K>.
- [38] Y. Qin et al., Ultrathin exfoliated  $\text{WS}_2$  nanosheets in low-boiling-point solvents for high-efficiency hydrogen evolution reaction, *IOP Conf. Ser.: Mater. Sci. Eng.* 770 012079. <https://doi.org/10.1088/1757-899X/770/1/012079>.
- [39] S.K. Balasingam, J.S. Lee, Y. Jun, Few-layered  $\text{MoSe}_2$  nanosheets as an advanced electrode material for supercapacitors, *Dalton Trans.* 44 (2015). <https://doi.org/10.1039/C5DT01985K>.
- [40] P. Tonndorf, R. Schmidt, P. Böttger, et al., Photoluminescence emission and Raman response of monolayer  $\text{MoS}_2$ ,  $\text{MoSe}_2$ , and  $\text{WSe}_2$ , *Opt. Express* 21 (2013) 4908–4916. <https://doi.org/10.1364/OE.21.004908>.
- [41] Ž. Petrović, M. Ristić, S. Musić, M. Fabian, The effect of GA on the nano/microstructure and optical properties of precipitated  $\text{ZnO}$ , *Croat. Chem. Acta* 90 (2017). <https://doi.org/10.5562/cca3121>.
- [42] R.C. Quintanilha, E.S. Orth, A. Grein-Iankovski, I.C. Riegel-Vidotti, M. Vidotti, The use of GA as “green” stabilizer of poly(aniline) nanocomposites: A comprehensive study of spectroscopic, morphological and electrochemical properties, *J. Colloid Interface Sci.* 434 (2014). <https://doi.org/10.1016/j.jcis.2014.08.006>.
- [43] M.A. Rabeea, R.H. Daoub, A.H. Elmubarak, et al., Characterization and functional properties of some natural Acacia gums, *J. Saudi Soc. Agric. Sci.* 17 (2018) 105–114. <https://doi.org/10.1016/j.jssas.2016.05.002>.

- [44] O.M. Lemine, N. Ahmad, M. Alshammari, et al., Maghemite ( $\gamma$ -Fe<sub>2</sub>O<sub>3</sub>) and  $\gamma$ -Fe<sub>2</sub>O<sub>3</sub>-TiO<sub>2</sub> nanoparticles for magnetic hyperthermia applications: synthesis, characterization and heating efficiency, *Materials* 14 (2021) 5691. <https://doi.org/10.3390/ma14195691>.
- [45] H. Shokrollahi, A review of the magnetic properties, synthesis methods and applications of maghemite, *J. Magn. Magn. Mater.* 426 (2017) 74-81. <https://doi.org/10.1016/j.jmmm.2016.11.033>.
- [46] E. Mosiniewicz-Szablewska, A. Tedesco, P. Suchocki, et al., Magnetic studies of polylactic-co-glycolic acid nanocapsules loaded with selol and  $\gamma$ -Fe<sub>2</sub>O<sub>3</sub> nanoparticles, *Phys. Chem. Chem. Phys.* 22 (2020) 21042-21058. <https://doi.org/10.1039/D0CP02706E>.
- [47] M.M. Hussein, H.F. Saafan, H.F. Abosheish, et al., Preparation, structural, magnetic, and AC electrical properties of synthesized CoFe<sub>2</sub>O<sub>4</sub> nanoparticles and its PVDF composites, *Mater. Chem. Phys.* 317 (2024) 129041. <https://doi.org/10.1016/j.matchemphys.2024.129041>.
- [48] C. Sun, J.S.H. Lee, M. Zhang, Magnetic nanoparticles in MR imaging and drug delivery, *Adv. Drug Deliv. Rev.* 10 (2008) 1234-1245. <https://doi.org/10.1016/j.addr.2008.03.018>
- [49] A. Włodarczyk, S. Gorgon, A. Radoń, K. Bajdak-Rusinek, Magnetite nanoparticles in magnetic hyperthermia and cancer therapies: challenges and perspectives, *Nanomaterials* 12 (2022) 1807. <https://doi.org/10.3390/nano12111807>.
- [50] Marroquin, J.F.R., Ghiglieno, F., Archanjo, B.S., Roncaratti, L.F., Felix, J.F., Defect engineering via gamma irradiation in scalable mechanical exfoliation TMDs thin films for improved electrocatalytic hydrogen evolution, *Chemical Engineering Journal* 498 (2024), <https://doi.org/10.1016/j.cej.2024.155498>.
- [51] O. Lanier, O. Korotych, A. Monsalve, et al., Evaluation of magnetic nanoparticles for magnetic fluid hyperthermia, *Int. J. Hyperthermia* 36 (2019) 687-701. <https://doi.org/10.1080/02656736.2019.1628313>.
- [52] Mehdaoui, B. et al., Increase of magnetic hyperthermia efficiency due to dipolar interactions in low-anisotropy magnetic nanoparticles: Theoretical and experimental results, *Phys. Rev. B* 87 (2013) 174419. <https://doi.org/10.1103/PhysRevB.87.174419>.

[53] Jiananda, A., Sari, E.K., Larasati, D.A., Tumbelaka, R.M., Ardiyanti, H., Darmawan, M.Y., Istiqomah, N.I., Sunaryono, Wicaksono, S.T., Suharyadi, E., Optical, microstructural, and magnetic hyperthermia properties of green-synthesized Fe<sub>3</sub>O<sub>4</sub>/carbon dots nanocomposites utilizing Moringa oleifera extract and watermelon rinds, *Carbon Trends* 13 (2023) 100305. <https://doi.org/10.1016/j.cartre.2023.100305>.

[54] El-Boubbou, K., Lemine, O. M., Algessair, S., Madkhali, N., Al-Najar, B., AlMatri, E., Ali, R., & Heninie, M. (2024). Preparation and characterization of various PVPylated divalent metal-doped ferrite nanoparticles for magnetic hyperthermia. *RSC Advances* 14, 15664–15679. <https://doi.org/10.1039/d4ra01600a>.